THE JOURNAL OF PHYSICAL CHEMISTRY Letters

Letter

Cite This: J. Phys. Chem. Lett. 2018, 9, 3969−3977

pubs.acs.org/JPCL

Activation Energy of Organic Cation Rotation in $CH_3NH_3PbI_3$ and $CD_3NH_3PbI_3$: Quasi-Elastic Neutron Scattering Measurements and First-Principles Analysis Including Nuclear Quantum Effects

Jingrui Li,[*,†,∥] Mathilde Bouchard,[‡,∥] Peter Reiss,[‡] Dmitry Aldakov,[‡] Stéphanie Pouget,[‡] Renaud Demadrille,[‡] Cyril Aumaitre,[‡] Bernhard Frick,[¶] David Djurado,[*,‡] Mariana Rossi,[*,§,∥] and Patrick Rinke[†]

[†]Department of Applied Physics, Aalto University, P.O. Box 11100, FI-00076 Aalto, Finland

[‡]Université Grenoble-Alpes, CEA, CNRS, INAC/SyMMES, CEA Grenoble, 17 Avenue des Martyrs, 38054, Grenoble, France

[¶]Institut Laue Langevin, 71 Avenue des Martyrs, 38042, Grenoble, France

[§]Fritz Haber Institute of the Max Planck Society, Theory Department, Faradayweg 4-6, D-14195 Berlin, Germany

Supporting Information

ABSTRACT: The motion of $CH_3NH_3^+$ cations in the low-temperature phase of the promising photovoltaic material methylammonium lead triiodide ($CH_3NH_3PbI_3$) is investigated experimentally as well as theoretically, with a particular focus on the activation energy. Inelastic and quasi-elastic neutron scattering measurements reveal an activation energy of ∼48 meV. Through a combination of experiments and first-principles calculations, we attribute this activation energy to the relative rotation of CH_3 against an NH_3 group that stays bound to the inorganic cage. The inclusion of nuclear quantum effects through path integral molecular dynamics gives an activation energy of ∼42 meV, in good agreement with the neutron scattering experiments. For deuterated samples ($CD_3NH_3PbI_3$), both theory and experiment observe a higher activation energy for the rotation of CD_3 against NH_3, which results from the smaller nuclear quantum effects in CD_3. The rotation of the NH_3 group, which is bound to the inorganic cage via strong hydrogen bonding, is unlikely to occur at low temperatures due to its high energy barrier of ∼120 meV.

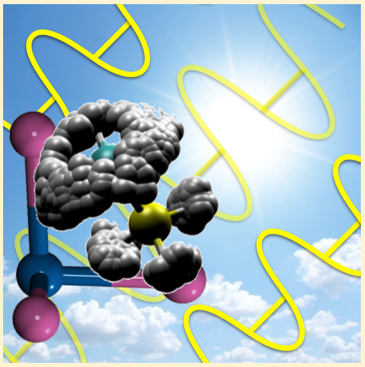

Hybrid perovskite photovoltaic (HPPV) technology[1,2] has received rapidly increasing interest from the emerging solar-cell community due to its record increase in power-conversion efficiency (PCE) during the last 5 years. The current state-of-the-art HPPV architecture was proposed in 2012, achieving ∼10% PCE at the time.[3,4] With the advancement of materials design and synthesis, the PCE of HPPV cells has already reached 22%, overtaking the best-performing inorganic-based single-junction thin-film cells. The most common photoactive material in HPPV cells is methylammonium (MA ≡ CH_3NH_3) lead triiodide ($CH_3NH_3PbI_3$, shortened as $MAPbI_3$ hereafter). This material combines many advantageous features for photovoltaic applications, e.g., optimal band gap for single-junction solar-cell absorbers,[5] excellent absorption strength in the visible part of the solar spectrum,[6] and high mobilities for both electron and hole transport.[7,8] Moreover, hybrid perovskites can be synthesized in solution at low temperature from common materials. Therefore, HPPV cells have become promising candidates for clean, affordable, and sustainable energy generation.

Despite its promises, many fundamental materials characteristics of $MAPbI_3$ remain poorly understood. Recent experimental and theoretical studies focused on the device architecture and performance,[9−11] different hybrid-perovskite compositions,[5,12−14] the large diffusion-lengths and low recombination rate,[7,8,15,16] the current−voltage hysteresis,[5,17−19] and the stability of hybrid perovskites materials.[20−22] The microstructure of $MAPbI_3$, which is crucial for the initial stages of the light-to-energy conversion process in particular the generation and separation of an electron−hole pair, has received little attention. Although first-principles studies have already revealed that the organic MA^+ cations are bound to the inorganic cage via hydrogen bonding between the NH_3 group and halide anions,[23,24] information on the motion of the MA^+ cations remains controversial. There are two conflicting viewpoints: (1) The MA^+ cations can move nearly freely at high temperatures,[25,26] because only a small activation energy (E_a) is required for the cleavage of the hydrogen bonds.[27,28] (2) The MA^+ cations are fixed in stable orientations, because E_a is of the order of 100 meV.[29−33]

In this letter, we address the question of MA^+ rotation by combining quasi-elastic neutron scattering (QENS) experi-

Received: April 26, 2018
Accepted: June 30, 2018
Published: July 1, 2018

ments with first-principles density-functional theory calculations. With QENS measurements we study MA-motion in the low-temperature (<160 K) orthorhombic phase of $MAPbI_3$. QENS is very sensitive to incoherent scattering events involving hydrogen nuclei. It is thus the ideal tool to study the motion of $CH_3NH_3^+$.

In previous $MAPbI_3$ QENS studies, Leguy et al. measured E_a to be 9.9 meV[27] and Chen et al. 48 meV.[32] Both did not consider the difference between the axial rotation (that is, the rotation around the C−N bond) of only the methyl (Me ≡ CH_3) group and that of the whole MA^+ cation. In this work, we studied the local dynamics of MA^+ cations in $MAPbI_3$ powder samples at temperatures <160 K using incoherent QENS. To better understand the rotation mechanism, we also performed QENS on samples with deuterated methyl groups ($CD_3NH_3PbI_3$). If deuteration changed E_a, it would indicate that the rotation would mainly involve the methyl group but not the ammonium group. In such a case, CH_3 rotates relative to the NH_3 group, which in our picture would remain hydrogen-bonded to the inorganic cage.

To obtain an in-depth understanding of the fundamental atomic processes in $MAPbI_3$, we performed first-principles density-functional theory (DFT) calculations for different MA^+ rotations. For each rotation process, we first mapped the potential energy surface onto a 1D hindered-rotor model to extract the barriers. We then performed *ab initio* path integral molecular dynamics (PIMD) calculations that include nuclear quantum effects beyond the 1D model to better characterize the free energy surface from which an estimate of E_a can be extracted. From the calculated activation energies, we can directly estimate whether a dynamical process is likely to occur at a certain temperature.

Neutron Scattering Experiments. We carried out different types of neutron scattering experiments on powder samples of $CH_3NH_3PbI_3$ and its partly deuterated analogue $CD_3NH_3PbI_3$ using the backscattering spectrometer IN16B at the Laue-Langevin Institute in Grenoble. The incoherent neutron scattering cross section of ^1H is 80.2 b. It provides the major contribution to the total (coherent and incoherent) neutron scattering cross section of both samples. The coherent contribution from ^1H is 1.8 b. For comparison, the coherent and incoherent neutron scattering cross section of D ≡ ^2H are 5.6 and 2.0 b, respectively. As a result, the total neutron scattering cross section of $CH_3NH_3PbI_3$ is 523.9 b, much larger than $CD_3NH_3PbI_3$ (300.7 b). These two samples have quite similar total absorption cross sections (10.8 and 9.8 b for $CH_3NH_3PbI_3$ and $CD_3NH_3PbI_3$, respectively) and nearly the same density. Thus, for similar absorption power, the total neutron scattering power of $CH_3NH_3PbI_3$ is larger than $CD_3NH_3PbI_3$ by a factor of 1.69.

The chemical synthesis and nuclear magnetic resonance (NMR) characterization of samples are described in Section S1 of the Supporting Information. The principles and details of our neutron scattering measurements are given in Section S2 of the Supporting Information. Three types of neutron scattering measurements (elastic, inelastic, and quasi-elastic) were carried out and will be discussed in this letter.

First, we performed elastic fixed window scans (EFWS) for a quick overview of the onsets of motions that are faster than the time scale corresponding to the energy resolution. The temperature-resolved results are given in Figure 1. Panel a shows a ratio of 1.48 for the elastic scattering intensity between the hydrogenated and the deuterated samples at a very low

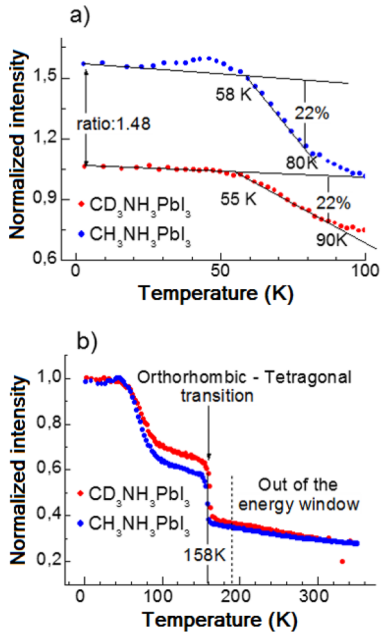

Figure 1. Elastic fixed window scans (with summing over all selected Q values, see Section S2 of the Supporting Information) of $CH_3NH_3PbI_3$ (blue) and $CD_3NH_3PbI_3$ (red): (a) at low temperatures (3, 130) K and (b) within the whole scanned temperature range (3, 350) K with intensities normalized according to that obtained at 3 K.

temperature (2 K), where all rotational motions are frozen. This ratio does not deviate much from the aforementioned theoretical ratio of 1.69. ^1H NMR spectroscopy obtained after the drying process of the deuterated sample clearly confirmed that the deuteration rate is 99% (see Figure S1 of the Supporting Information).

EFWS is a recording of the integrated intensities of elastic scattering events. Their attenuation with increasing temperature is described by the Debye−Waller factor

$$S(\mathbf{Q}) = C\, e^{-Q^2\langle u^2\rangle/3} \quad (1)$$

where S is the elastic scattering function, C a constant, $\mathbf{Q}$ the scattering vector, and $\boldsymbol{u}$ the displacement of the scatterers. Figure 1a shows that the mean square displacement $\langle u^2\rangle$ decreases (approximately) linearly for temperatures lower than 58 and 55 K for the all-protonated and deuterated perovskites, respectively. At higher temperatures, the quasi-elastic component of scattering becomes visible within the resolution of the spectrometer. It broadens the scattering function and accordingly the elastic intensity decreases more rapidly, as shown in Figure 1a. This broadening increases with temperature. Above a certain temperature (80 K for $CH_3NH_3PbI_3$ and 90 K for $CD_3NH_3PbI_3$), it becomes too large to be accurately measured (see Figure S3 of the Supporting Information). At this point, the investigated motion becomes so rapid that its quasi-elastic contribution does only weakly contribute to the elastic intensity by its amplitude. Figure 1a shows that the elastic intensity decreases in the same proportion for the two compounds within the respective temperature ranges where the elastic intensity is most sensitive to the change of the quasi-elastic broadening. This may suggest that the local dynamics involved in these two compounds have the same characteristics.

DOI: 10.1021/acs.jpclett.8b01321
J. Phys. Chem. Lett. 2018, 9, 3969−3977

A scan over a larger temperature range is given in Figure 1b, in which the scattering intensity of $CD_3NH_3PbI_3$ is normalized to that of $CH_3NH_3PbI_3$ at low temperatures. The data illustrates that at temperatures lower than the orthorhombic-tetragonal phase transition at ∼160 K, these two samples exhibit a similar behavior, with the remaining scattering intensity of $CD_3NH_3PbI_3$ noticeably higher than its all-protonated analogue. It also exhibits that the elastic-intensity decrease becomes slower between 80 and 150 K (before the orthorhombic-tetragonal phase transition at ∼160 K). We have examined this behavior carefully by studying the character of the elastic incoherent structure factor (EISF) and present our analysis in detail in Section S2 (Figures S4−S6) of the Supporting Information. Our analysis supports the assumption that the local dynamics mainly involve the rotation of only the methyl group (while the ammonium rotor remains bound to the inorganic framework via hydrogen bonds). The objective of this work is to couple neutron scattering analysis with first-principles calculations of the atomic structure and potential energy surfaces (in the next section) to verify this assumption.

Next we discuss the inelastic fixed window scans (IFWS). Figure 2 shows the results for the normalized intensities of

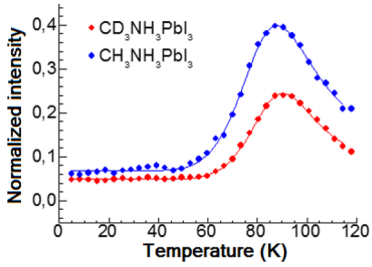

Figure 2. Inelastic fixed window scans of $CH_3NH_3PbI_3$ (blue) and $CD_3NH_3PbI_3$ (red). The fits using eq 2a are given in solid lines.

$CD_3NH_3PbI_3$ scaled by a factor of 1.48. Both data exhibit a quasi-plateau at temperatures lower than 50 K, an increase from about 50 K, and a maximum at 85−90 K, where the peak of the all-protonated system is higher. For a quantitative analysis, we fit the IFWS data with eq 2a following ref 34 and show the results in Figure 2 with solid lines. Specifically, eq 2a describes the relationship between the scattering intensity I^{IFWS} and relaxation time τ at a given temperature T and energy window ω_{off}. We assume that the dynamics follows a stochastic process so that it can be described by eq 2b (Arrhenius equation), where k_B is the Boltzmann constant. The temperature at which I^{IFWS} takes its maximum can be calculated by eq 2c. The fitted activation energy results are listed in Table 1. We will discuss them together with the quasi-elastic measurement results.

$$I^{IFWS} \propto \frac{\tau(T)}{1 + \omega_{off}^2 \tau^2(T)} \quad (2a)$$

$$\tau(T) = \tau_0 \, e^{E_a/k_B T} \quad (2b)$$

$$T_{max} = -\frac{E_a}{k_B \log(\omega_{off}\tau_0)} \quad (2c)$$

To check the consistency of our IFWS E_a results, we also carried out quasi-elastic measurements at different scattering vectors and temperatures. Figure 3 shows that, for both samples in the low-temperature range, the logarithm of the

Table 1. Activation Energy (E_a) and Pre-Exponential Factor (τ_0) of MA-Motion in Low-Temperature $CH_3NH_3PbI_3$ and $CD_3NH_3PbI_3$ Obtained by Fitting Inelastic (IE) and Quasi-Elastic (QE) Neutron Scattering Data[a]

		$CH_3NH_3PbI_3$	$CD_3NH_3PbI_3$
T_{max} [K]	IE	87.9 ± 0.4	90.3 ± 0.3
E_a [meV]	IE	46.9 ± 1.3	57.5 ± 0.7
	QE	48.2 ± 3.9	53.8 ± 7.5
τ_0 [fs]	IE	688 ± 122	205 ± 14
	QE	403 ± 270	1540 ± 410

[a]Also listed are the maximal IE-intensity temperature (T_{max}).

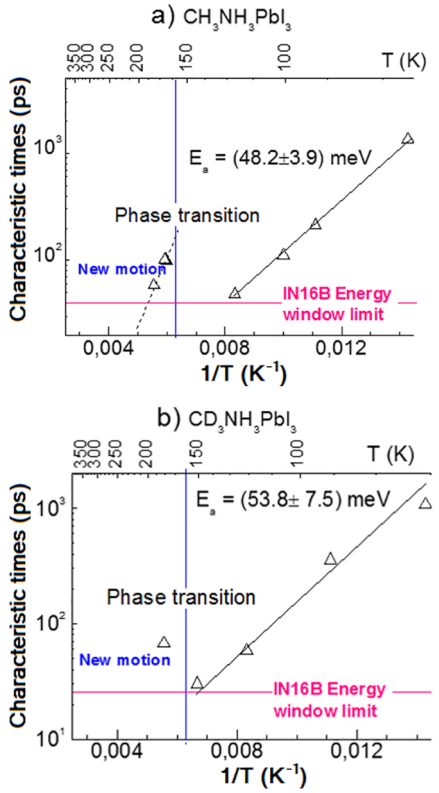

Figure 3. Arrhenius plot (relaxation time vs temperature) of (a) $CH_3NH_3PbI_3$ and (b) $CD_3NH_3PbI_3$ from quasi-elastic neutron scattering at low temperatures. Activation energies (E_a) are listed in the plot.

relaxation time depends linearly on the inverse temperature. By fitting these data with the Arrhenius equation, we calculated the activation energies of MA-motion in both cases. The results are indicated in Figure 3 and listed in Table 1. Note: the signal-to-noise ratio in the spectra recorded for $CD_3NH_3PbI_3$ is much lower than those for $CH_3NH_3PbI_3$, as presented in Section S2 of the Supporting Information.

Table 1 illustrates that IFWS and quasi-elastic measurements produce E_a values in good agreement with each other for both all-protonated and partly deuterated $MAPbI_3$. We thus claim that IFWS is an appropriate tool for the study of local dynamics in $MAPbI_3$. Specifically, the fitted E_a for low-temperature $CH_3NH_3PbI_3$ is 47−48 meV, agreeing well with previous QENS results (48 meV).[32] The activation energy of local dynamics in the deuterated sample is larger than in the all-protonated one by 6 meV (quasi-elastic) or 11 meV (IFWS). The good agreement of this fit with the data indicates that the process is thermally activated. Thus, we can expect

DOI: 10.1021/acs.jpclett.8b01321
J. Phys. Chem. Lett. 2018, 9, 3969−3977

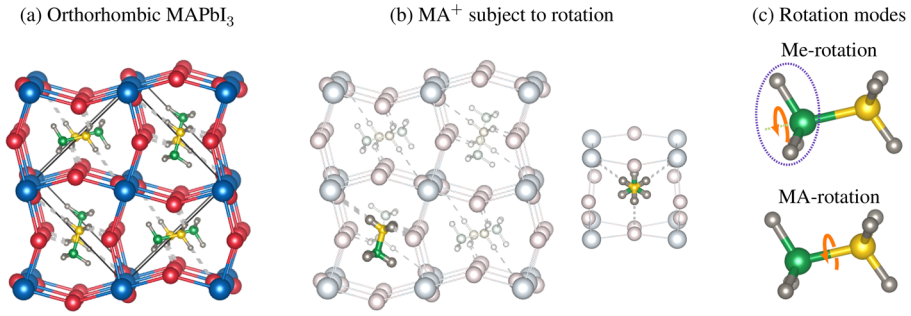

Figure 4. (a) Optimized structure of the orthorhombic $\sqrt{2} \times \sqrt{2} \times 2$ supercell (unit-cell edges marked by black lines) of $MAPbI_3$. Here we duplicated it to a $2 \times 2 \times 2$ right rhombic prism supercell. (b) Starting geometry for the investigated processes. Left: the rotated MA^+ cation is highlighted, while the rest part of the supercell is shown in a lighter shade; right: Newman projection of the rotating MA^+. (c) Investigated rotation modes of MA^+ in the orthorhombic $MAPbI_3$ structure: Me-rotation (upper panel) and MA-rotation (lower panel). C, N, H, Pb, and I atoms are colored in green, yellow, dark gray, blue, and red, respectively. The hydrogen bonds between H atoms in the NH_3 group and I^- anions are emphasized by gray dashed lines.

that the main contribution to the observed isotope effects comes from zero-point-energy.

Based on our elastic and inelastic measurements, we can already conjecture the atomistic origin of the local dynamics in the low-temperature phase of $MAPbI_3$. As alluded to before, Chen et al. claimed that both CH_3 and NH_3 rotors participate in a rotation of the MA^+ cation.[32] However, considering the discussion of the EISF evolution (see Section S2 of the Supporting Information for details), we instead propose that only CH_3 rotors move for the following reasons. First, as the H atoms in the methyl group are not bound to the inorganic cage with hydrogen bonding, we should obtain similar E_a as found in many other systems where CH_3 rotors are present. Actually, our E_a of 47−48 meV is close to the QENS results of Me-side-group rotation in polymers (5.3 kJ mol^{-1} = 55 meV).[35] Second, the activation energy of $CD_3NH_3PbI_3$ and $CH_3NH_3PbI_3$ noticeably differ. In the following, we will support our conjecture with first-principles calculations that provide a precise atomistic picture.

First-Principles Density-Functional-Theory Calculations. To model the MA-motion in the orthorhombic phase of $MAPbI_3$, we carried out first-principles (DFT) calculations on a series of model systems. The lattice parameters were adopted from single-crystal X-ray-diffraction data a = 8.56 Å, b = 8.84 Å, and c = 12.58 Å.[12] They characterize a $\sqrt{2} \times \sqrt{2} \times 2$ supercell consisting of four single (quasi-primitive) cells. In each single cell, Pb^{2+} ions are located at the corners and I^- at the edge-centers. MA^+ cations, located close to the cell centers, take different (quasi-)face-to-face directions in different cells. Figure 4a depicts the DFT-relaxed atomic geometry (for a fixed size of unit cell marked by solid lines), which agrees well with previously reported DFT[33] and *ab initio* molecular dynamics[36] results. To reduce the coupling between nearest rotating MA^+ ions (that result from the periodic boundary conditions), we duplicated the orthorhombic $\sqrt{2} \times \sqrt{2} \times 2$ cell into a $2 \times 2 \times 2$ supercell, which contains eight single $MAPbI_3$ unit cells. Its lattice parameters are $a = b$ = 12.30 Å, c = 12.58 Å, and $\alpha = \beta = 90°$, $\gamma = 88.15°$. Only one of eight MA^+ ions (Figure 4b) is subject to the investigated rotations, which keeps it well separated from other rotating MA^+ in the bulk structure.

Figure 4c depicts the two rotation modes considered in this paper: For the Me-rotation in the upper panel, only the CH_3 group was rotated around the C−N bond, whereas for the MA-rotation in the lower panel the whole molecule was rotated around the C−N bond. The rotational angle is well-defined, even when we fully relax the geometry, as we treated the rotating part (CH_3 or NH_3) as a rigid body. According to the (quasi) C_{3v} symmetry of our model systems, we only scan over the rotational angle range (0,120)°. We also fixed the length and the orientation of the C−N bond. Note: since CH_3 is only bonded to NH_3 but does not interact with the PbI_3^- framework via hydrogen bonding, we supposed that it will follow the NH_3 rotation. NH_3 rotation is therefore equivalent to MA^+ rotation, as demonstrated by our results.

We did not explicitly consider the flip of the whole MA molecule, i.e., a rotation of the NH_3 group around the C−N bond center. Chen et al. had ruled this process out in the low-temperature phase of $MAPbI_3$.[32] Their assessment agrees with our own EFWS results and with test calculations reported in Section S3 of the Supporting Information and in our forthcoming publication.

In our DFT calculations, we used the Perdew−Burke−Ernzerhof (PBE)[37] exchange-correlation functional augmented with long-range van der Waals (vdW) corrections based on the Tkatchenko−Scheffler method.[38] In addition, scalar relativistic effects were included by means of the zero-order regular approximation (ZORA).[39] Our previous study[24] demonstrated that this approach gives lattice constants of hybrid perovskites in good agreement with experiment and can appropriately describe the interaction between the organic cations and the inorganic framework. For a more accurate electronic structure, the total energy of each PBE+vdW relaxed geometry was calculated using the hybrid "PBE0+vdW" functional.[40]

All DFT calculations in this work were performed with the all-electron numeric-atom-centered orbital code FHI-aims.[41−44] For all calculations we used tier 2 basis sets. A Γ-centered $6 \times 6 \times 4$ k-point mesh was used for the optimization of the orthorhombic $\sqrt{2} \times \sqrt{2} \times 2$ supercell structure, and a $4 \times 4 \times 4$ k-point mesh for the $2 \times 2 \times 2$ supercell models. For the path integral molecular dynamics (PIMD) simulations, we employed the interface of FHI-aims with the i-PI[45] code. The PIMD calculations were run in a cluster model, in which a single PbI_3^- unit was held fixed in its bulk position and the $CH_3NH_3^+$ and $CD_3NH_3^+$ molecules were allowed to move freely. The simulation was run at 150 K with 12 beads and the PIGLET thermostat.[46] The results of all relevant calculations of this work are available from the Novel Materials Discovery (NOMAD) repository.[47]

DOI: 10.1021/acs.jpclett.8b01321
J. Phys. Chem. Lett. 2018, 9, 3969−3977

We start the presentation of our DFT results with the Me-rotation. The PBE+vdW relaxed structures at several rotation angles (30, 60, and 90°) of this process are shown in Figure 5.

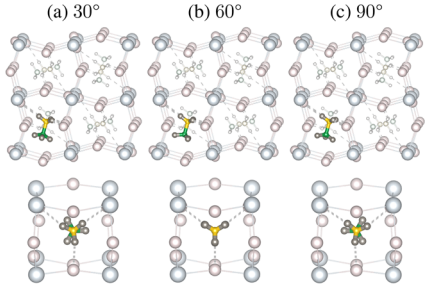

Figure 5. Optimized structures at several Me-rotational angles: (a) 30°, (b) 60°, and (c) 90°. Upper panel: atomic structure of the whole unit cell. Lower panel: Newman projection of the rotating MA^+ and the surrounding inorganic framework.

During the rotation of the CH_3 group, the rest of the supercell (shown in light colors) remains largely unaffected. A clearer view is given by the Newman projection in the lower panel. As the CH_3 group rotates from the "staggered" (0°, i.e., the fully relaxed structure shown in Figure 4b) to the "eclipse" (60°, Figure 5b) configuration, the location of the NH_3 group and the surrounding inorganic cage remain nearly unchanged. We can thus conclude that the force on NH_3 induced by the torsion around the C−N single bond is much weaker than that related to the hydrogen-bonding interaction with the inorganic framework.

In Figure 6 we plot the potential energy surface (PES) for Me-rotation with both PBE+vdW and PBE0+vdW. For clarity,

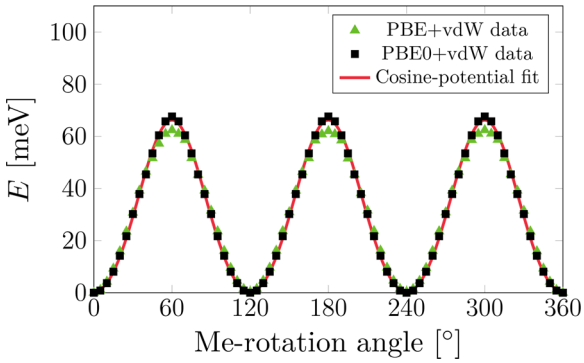

Figure 6. PES for Me-rotation. The PBE+vdW total-energy data is plotted with green triangles, PBE0+vdW with black squares, and the fitted cosine-potential to the PBE0+vdW results in red.

we set the total energy of the 0°-structure to 0 and shifted all other data accordingly. The PBE+vdW PES (green triangles in Figure 6) exhibits three minima of equal-height. They are located at 0 (360), 120, and 240°, where the CH_3 and NH_3 take the staggered configuration in the Newman projection. There are three corresponding equal-height maxima (62 meV) at 60, 180, and 300° that each exhibit eclipsed H atoms. The PBE+vdW total energies of Me-rotation can be perfectly characterized by a cosine function with period 120° (see Section 4 of the Supporting Information). This reflects the nearly perfect C_{3v} symmetry of the Me group, which is not noticeably perturbed by inhomogeneous interactions with the inorganic framework. PBE0+vdW gives an equivalent PES (black squares in Figure 6) with slightly higher (by 5 meV) barriers, i.e., torsion energies for the C−N bond.

Now we turn to MA-rotation. Figure 7 shows the PBE+vdW relaxed structures at several rotation angles of NH_3 around the

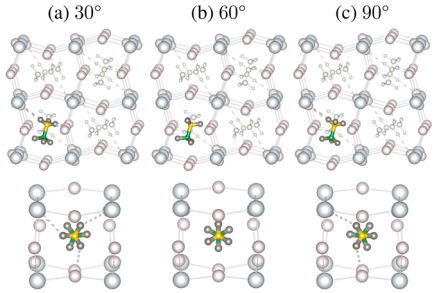

Figure 7. Optimized structures at several MA-rotational angles: (a) 30°, (b) 60°, and (c) 90°. Upper panel: atomic structure of the whole unit cell. Lower panel: Newman projection of the rotating MA^+ and the surrounding inorganic framework.

C−N bond. It indicates the major difference between CH_3 and NH_3 rotation: while Me-rotation does not affect the NH_3 group, NH_3 rotation forces CH_3 to follow the rotation via the torsion potential. This effectively results in the rotation of the whole $CH_3NH_3^+$ ion, which maintains the staggered configuration of H atoms during the whole process as reflected by the Newman projections (lower panel of Figure 7a−c). Such a rotation causes the cleavage of H···I hydrogen bonds, which, according to our previous study,[24] would have significant impact on the inorganic-framework deformation (the "chicken-and-egg" interplay). However, since the other seven MA^+ ions are held fixed in our calculations, the PbI_3^- cage cannot deform significantly, as is also seen in Figure 7.

Figure 8 depicts the PBE+vdW and PBE0+vdW PESs. They exhibit similar features. The PBE+vdW PES (green triangles in

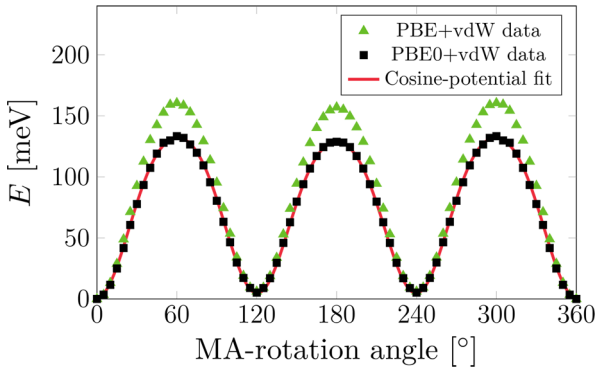

Figure 8. PES for MA-rotation. The PBE+vdW total-energy data is plotted with green triangles, PBE0+vdW with black squares, and the fitted cosine-potential to the PBE0+vdW results in red.

Figure 8) has a barrier of 161 meV from 0 to 60°. This corresponds to a breaking of all three hydrogen bonds (Figure 7b). Unlike for Me-rotation, the inclusion of exact exchange in the density functional has a large effect on this MA-rotation (black squares in Figure 8), as it results in a noticeably lower barrier (by 28 meV).

To summarize, the interaction energies between the inorganic PbI_3^- cage, the CH_3 group, and the NH_3^+ part of an organic MA^+ ion, has the following order:

DOI: 10.1021/acs.jpclett.8b01321
J. Phys. Chem. Lett. 2018, 9, 3969−3977

$$V(PbI_3^-{-}CH_3) \ll V_{torsion}(CH_3{-}NH_3^+) < V(PbI_3^-{-}NH_3^+)$$

The major contribution for $V(PbI_3^-{-}CH_3)$ includes vdW interactions and ionic bonding (the positive charge of MA^+ is partially distributed over Me). Both are almost not affected by either Me- or MA-rotation. $V(PbI_3^-{-}NH_3^+)$ includes vdW interactions, ionic bonding, and hydrogen bonding. MA-rotation has significant impact on the last component. Note: $V_{torsion}(CH_3{-}NH_3^+)$ is only related to the torsion around the C−N bond but not the covalent bonding itself.

Analysis of Rotational Potential Energy Surfaces Using a One-Dimensional Hindered-Rotor Model. From our DFT (PBE/PBE0+vdW) calculations, we have obtained PESs for both Me- and MA-rotation. They provide us with insight (e.g., energy barriers) into the associated processes. To calculate activation energies, we also need to consider zero-point-energy (ZPE) related to the quantum-mechanical vibrational ground-state energy of the associated PES.

Both Me and MA PESs exhibit a periodic and even function. In general, such a function can be expanded in terms of a cosine series in the rotational angle, here θ:

$$V(\theta) = \frac{v_0}{2} + \sum_{n=1}^{+\infty} v_n \cos(n\theta),$$
$$\forall\, n \geqslant 1, \quad v_n = \frac{1}{\pi}\int_0^{2\pi} V(\theta)\cos(n\theta)\,\mathrm{d}\theta \tag{3}$$

Here the period of $V(\theta)$ is 360° (2π). V represents the potential energy for a generalized hindered rotor.

By projecting the PBE0+vdW PES of Me- and MA-rotation onto the cosine functions $\cos(n\theta)$ with positive integer numbers n, we only obtained non-negligible coefficients for a few terms (apart from the constant term $\frac{v_0}{2}$): $v_3 = -32.9$ meV,$v_6 = 2.0$ meV for Me-rotation, and $v_2 = -2.2$ meV,$v_3 = -63.7$ meV,$v_6 = -6.2$ meV for MA-rotation. In both cases, we set the constant term for $V(0) = 0$. The fitted PESs are presented by the red curves in Figures 6 and 8.

The Hamiltonian for the system subject to the generalized-hindered-rotor potential V (eq 3) reads

$$\hat{H} = -\frac{\hbar^2}{2I}\frac{\mathrm{d}^2}{\mathrm{d}\theta^2} + V(\theta) \tag{4}$$

We can calculate the moment of inertia I from the DFT-relaxed atomic structure (Figure 4a). For Me-rotation, we have $I = 3.24$ u Å^2 (note, the NH_3 part is not included here as its geometry nearly remains unchanged), which is close to the experimental value of 3.185 u Å^2 obtained from rotational spectroscopy experiments of Me-rotation in the isolated CH_3NH_2 molecule.[48] For MA-rotation, in which all 6 H atoms contribute, we have 6.11 u Å^2.

The time-independent Schrödinger equation

$$\left\{-\frac{\hbar^2}{2I}\frac{\mathrm{d}^2}{\mathrm{d}\theta^2} - \sum_n v_n[1-\cos(n\theta)]\right\}\psi_j(\theta) = E_j\psi_j(\theta) \tag{5}$$

has the form of a Mathieu equation and can be solved numerically.

By solving the eigenvalue problem eq 5 at 0 K, we calculated the ZPEs of Me- and MA-rotation, respectively. From this we obtain an estimate of the activation energy (note that our activation energy only includes enthalpic contributions and no entropy) by subtracting the ZPE from the energy barrier. Since we model this as a 1D reaction, only the 1D ZPE on the reactant state needs to be included. The details of solving the Mathieu equations eq 5 are given in Section S5 of the Supporting Information. Here we list the results in Table 2.

Table 2. Results of One-Dimensional Hindered-Rotor-Model Approach to Me- and MA-Rotation (In the Left and Right Sides, Respectively)[a]

Me group	I	ZPE	E_a	MA group	I	ZPE	E_a
CH_3	3.24	10.3	55.5	CH_3NH_3	6.11	11.4	119.3
CH_2D	4.32	9.0	56.8	CD_3NH_3	8.97	9.4	121.3
CHD_2	5.40	8.1	57.7	CH_3ND_3	9.35	9.3	121.5
CD_3	6.48	7.4	58.4	CD_3ND_3	12.21	8.1	122.6

[a]Listed are the moments of inertia I (in u Å^2), the calculated zero-point-energy (ZPE), and activation energy E_a (both in meV). Also different deuterated cases are included for each rotation mode.

The ZPEs of CH_3- and CH_3NH_3-rotation are 10.3 and 11.4 meV, respectively. Accordingly, the 1D hindered-rotor-model activation energies are 55.5 meV for CH_3-rotation and 119.3 meV for CH_3NH_3-rotation. The energy required to break the H···I hydrogen-bonds is thus much larger than to rotate the CH_3 or CD_3 group around the C−N bond.

Our Me-rotation activation energy agrees well with the QENS measurement of the methyl side group rotation in polymers (55 meV).[35] It is also very close to our QENS result (Arrhenius fit) of 48 meV for low-temperature $MAPbI_3$. This activation energy had previously been ascribed to MA-rotation,[32] for which our calculations produce a significantly higher activation energy of 119.3 meV. Therewith the possibility of MA-rotation to occur at <160 K is very low. For example, our simulation indicates that the number of MA-rotation events would be ∼500 times less than the number of Me-rotation events at 150 K and would happen <10 times in 1 ns. Section S6 of the Supporting Information summarizes our analysis.

Table 2 also lists our E_a estimates for the rotation of several deuterated Me and MA groups. Deuteration does not change the electronic structure of the system. Only the moment of inertia increases, which subsequently leads to a smaller ZPE (see Section S5 of the Supporting Information). Accordingly, the activation energy increases with the number of D atoms in the rotational group. This trend can be observed for both Me and MA rotation listed in Table 2. Specifically, for fully deuterated Me, i.e., CD_3, our 1D hindered-rotor model approach results in an activation energy of ∼58 meV, agreeing well with our neutron scattering measurement results. Partially deuterated methyl groups have larger ZPEs than the fully deuterated CD_3. This will contribute to the lower-energy signals in the neutron scattering spectra of $CD_3NH_3PbI_3$.

Estimate of Activation Energies from Path Integral Molecular Dynamics. By means of path integral molecular dynamics (PIMD), we can estimate the activation barrier of the methyl group directly in three-dimensional space, without restricting ourselves to a 1D model. Due to the large computational cost of PIMD simulations, we here use a model, in which we consider an isolated system consisting of one PbI_3^- group cut out from the lattice with a methylammonium group attached to it. The PbI_3^- group is held fixed, while the MA^+ can move freely. Due to the absence

DOI: 10.1021/acs.jpclett.8b01321
J. Phys. Chem. Lett. 2018, 9, 3969−3977

of the rest of the solid, we expect the barriers to be slightly lower than what they would be in the solid. We performed 30 ps long PIMD simulations with the PBE+vdW functional (*tight* settings for basis sets and numerical parameters in FHI-aims) for the hydrogenated and the deuterated systems after equilibrating both structures at 150 K, a temperature that is low enough for the orthorhombic structure to be the most stable and high enough for the methyl group rotation to be activated. We then calculated the probability density P projected on the rotation angle θ of the methyl group and calculated free energies as $F(\theta,T) = -k_B T \ln[P(\theta)]$. During our simulations, we never observed the cleavage of an H-bond between the NH_3 group and the iodine atoms but instead a slight precession of the C−N bond.

As shown in Figure 9, from the free energy profiles we can estimate an activation energy of 42 ± 2 meV for CH_3NH_3 and

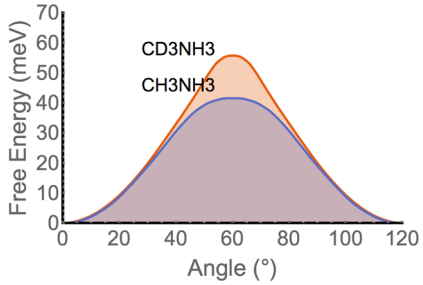

Figure 9. Free energy profiles for rotation of the CH_3 and the CD_3 group. The angle was measured as the dihedral angle defined by the H−C−N−H atoms. The simulation was run at 150 K.

of 56 ± 4 meV for CD_3NH_3, assuming a negligible contribution from tunneling effects. Our theoretical results are thus in excellent agreement with our neutron scattering results as alluded to earlier and the experimental results of ref 32. We predict a difference of around 10 meV in activation barriers between the all-protonated and the deuterated systems, which is solely due to the quantum nature of the nuclei. It is worth noting that this difference is more than double the one predicted for the simple 1D model presented in the last section. This difference is probably due to the coupling of this rotation mode to other vibrations of the molecule (most probably the CH/CD stretches), which go beyond the rigid rotor approximation. Regarding these bonds, we find that on average the CH bonds are 0.01 Å longer than the CD bonds in our PIMD simulations.

In conclusion, we investigated the motion of $CH_3NH_3^+$ cations in $CH_3NH_3PbI_3$ at low temperatures both experimentally and theoretically. By fitting our quasi-elastic neutron scattering data, we obtained an activation energy (E_a) of 48.2 meV, which agrees well with previous experiments.[32] Our experiments suggested that this E_a is associated with the rotation of only CH_3 rotors and does not involve NH_3 rotors. Our findings are corroborated by (a) the temperature and Q dependence of the incoherent elastic intensity and (b) the fact that neutron scattering of samples with deuterated methyl groups results in noticeably larger activation energies.

Theoretically, we modeled the rotation of CH_3 rotors using density functional theory and path integral molecular dynamics. For $CH_3NH_3PbI_3$, the prevalent nuclear quantum effects result in E_a = 42 meV for the rotation of the methyl group. This value agrees well with neutron scattering, with a small difference of several meV. For the deuterated (CD_3) rotors, we find much weaker nuclear quantum effects. The calculated E_a = 56 meV perfectly matches the value obtained from inelastic neutron scattering. We therefore ascribe the processes observed with neutron scattering at low temperatures to the rotation of only CH_3 around the C−N bond. Since the rotation of NH_3 breaks hydrogen bonds, its activation energy is much higher (∼120 meV) and the process has only minor contribution to the neutron-scattering intensities at the temperatures of our experiments.

Our study demonstrates that nuclear quantum effects are important for the motion of $CH_3NH_3^+$ cations in MA-based perovskites, inducing significant isotope effects. Our study provides important insight into the microstructure of $MAPbI_3$ that future research and device design can build on.

■ ASSOCIATED CONTENT

Supporting Information

The Supporting Information is available free of charge on the ACS Publications website at DOI: 10.1021/acs.jpclett.8b01321.

Synthesis and NMR characterization of studied samples, experimental conditions of neutron scattering measurements, additional data for DFT calculations of $MAPbI_3$ model systems, a brief analysis of the 1D hindered-rotor model, and theoretical estimation of possibility that CH_3NH_3-rotation occurs at low temperature (PDF)

■ AUTHOR INFORMATION

Corresponding Authors

*E-mail: jingrui.li@aalto.fi.
*E-mail: david.djurado@cea.fr.
*E-mail: rossi@fhi-berlin.mpg.de.

ORCID

Jingrui Li: 0000-0003-0348-068X
Peter Reiss: 0000-0002-9563-238X
Dmitry Aldakov: 0000-0002-4581-2462
Renaud Demadrille: 0000-0002-7455-5709

Author Contributions

‖J.L., M.B., and M.R. contributed equally to this work.

Notes

The authors declare no competing financial interest.
All experimental data obtained in the described measurements can be found under the following references: http://dx.doi.org/10.5291/ILL-DATA.7-04-139 and http://dx.doi.org/10.5291/ILL-DATA.7-04-140.

■ ACKNOWLEDGMENTS

We thank Dr. Claire Colin (Institut Néel−Grenoble) for her assistance for neutron scattering measurements on D2AM and D2A diffractometers at Institut Laue Langevin (ILL). ILL is acknowledged for beamtime allocation. The generous allocation of computing resources by the CSC-IT Center for Science (via the Project No. ay6311) and the Aalto Science-IT Project are gratefully acknowledged. An award of computer time was provided by the Innovative and Novel Computational Impact on Theory and Experiment (INCITE) program. This research used resources of the Argonne Leadership Computing Facility, which is a DOE Office of Science User Facility supported under Contract DE-AC02-06CH11357. This work was supported by "Agence Nationale pour le Recherche" via the project "Super Sans Plomb (2014−2018) and CEA (M.B.'s

DOI: 10.1021/acs.jpclett.8b01321
J. Phys. Chem. Lett. 2018, 9, 3969−3977

Ph.D. scholarship), the Collaborative Research Center (SFB) 951 of the German Science Foundation, and the Academy of Finland through its Centres of Excellence Programme (2012−2014 and 2015−2017) under Project Numbers 251748 and 284621, as well as its Key Project Funding scheme under Project Number 305632.

REFERENCES

(1) Snaith, H. J. Perovskites: The Emergence of a New Era for Low-Cost, High-Efficiency Solar Cells. *J. Phys. Chem. Lett.* **2013**, *4*, 3623−3630.
(2) Green, M. A.; Ho-Baillie, A.; Snaith, H. J. The Emergence of Perovskite Solar Cells. *Nat. Photonics* **2014**, *8*, 506−514.
(3) Kim, H.-S.; Lee, C.-R.; Im, J.-H.; Lee, K.-B.; Moehl, T.; Marchioro, A.; Moon, S.-J.; Humphry-Baker, R.; Yum, J.-H.; Moser, J. E.; et al. Lead Iodide Perovskite Sensitized All-Solid-State Submicron Thin Film Mesoscopic Solar Cell with Efficiency Exceeding 9%. *Sci. Rep.* **2012**, *2*, 591.
(4) Lee, M. M.; Teuscher, J.; Miyasaka, T.; Murakami, T. N.; Snaith, H. J. Efficient Hybrid Solar Cells Based on Meso-Superstructured Organometal Halide Perovskites. *Science* **2012**, *338*, 643−647.
(5) Stoumpos, C. C.; Malliakas, C. D.; Kanatzidis, M. G. Semiconducting Tin and Lead Iodide Perovskites with Organic Cations: Phase Transitions, High Mobilities, and Near-Infrared Photoluminescent Properties. *Inorg. Chem.* **2013**, *52*, 9019−9038.
(6) De Wolf, S.; Holovsky, J.; Moon, S.-J.; Löper, P.; Niesen, B.; Ledinsky, M.; Haug, F.-J.; Yum, J.-H.; Ballif, C. Organometallic Halide Perovskites: Sharp Optical Absorption Edge and Its Relation to Photovoltaic Performance. *J. Phys. Chem. Lett.* **2014**, *5*, 1035−1039.
(7) Stranks, S. D.; Eperon, G. E.; Grancini, G.; Menelaou, C.; Alcocer, M. J. P.; Leijtens, T.; Herz, L. M.; Petrozza, A.; Snaith, H. J. Electron-Hole Diffusion Lengths Exceeding 1 Micrometer in an Organometal Trihalide Perovskite Absorber. *Science* **2013**, *342*, 341−344.
(8) Xing, G.; Mathews, N.; Sun, S.; Lim, S. S.; Lam, Y. M.; Grätzel, M.; Mhaisalkar, S.; Sum, T. C. Long-Range Balanced Electron- and Hole-Transport Lengths in Organic-Inorganic $CH_3NH_3PbI_3$. *Science* **2013**, *342*, 344−347.
(9) Heo, J. H.; Im, S. H.; Noh, J. H.; Mandal, T. N.; Lim, C.-S.; Chang, J. A.; Lee, Y. H.; Kim, H.-j.; Sarkar, A.; Nazeeruddin, M. K.; et al. Efficient Inorganic-Organic Hybrid Heterojunction Solar Cells Containing Perovskite Compound and Polymeric Hole Conductors. *Nat. Photonics* **2013**, *7*, 486−491.
(10) Mei, A.; Li, X.; Liu, L.; Ku, Z.; Liu, T.; Rong, Y.; Xu, M.; Hu, M.; Chen, J.; Yang, Y.; et al. A Hole-Conductor-Free, Fully Printable Mesoscopic Perovskite Solar Cell with High Stability. *Science* **2014**, *345*, 295−298.
(11) Polander, L. E.; Pahner, P.; Schwarze, M.; Saalfrank, M.; Koerner, C.; Leo, K. Hole-Transport Material Variation in Fully Vacuum Deposited Perovskite Solar Cells. *APL Mater.* **2014**, *2*, 081503.
(12) Baikie, T.; Fang, Y.; Kadro, J. M.; Schreyer, M.; Wei, F.; Mhaisalkar, S. G.; Grätzel, M.; White, T. J. Synthesis and Crystal Chemistry of the Hybrid Perovskite $(CH_3NH_3)PbI_3$ for Solid-State Sensitized Solar Cell Applications. *J. Mater. Chem. A* **2013**, *1*, 5628−5641.
(13) Di Giacomo, F.; Razza, S.; Matteocci, F.; D'Epifanio, A.; Licoccia, S.; Brown, T. M.; Di Carlo, A. High Efficiency $CH_3NH_3PbI_{3-x}Cl_x$ Perovskite Solar Cells with Poly(3-hexylthiophene) Hole Transport Layer. *J. Power Sources* **2014**, *251*, 152−156.
(14) Weller, M. T.; Weber, O. J.; Henry, P. F.; Di Pumpo, A. M.; Hansen, T. C. Complete Structure and Cation Orientation in the Perovskite Photovoltaic Methylammonium Lead Iodide between 100 and 352 K. *Chem. Commun.* **2015**, *51*, 4180−4183.
(15) Ponseca, C. S., Jr.; Savenije, T. J.; Abdellah, M.; Zheng, K.; Yartsev, A.; Pascher, T.; Harlang, T.; Chabera, P.; Pullerits, T.; Stepanov, A.; et al. Organometal Halide Perovskite Solar Cell Materials Rationalized: Ultrafast Charge Generation, High and Microsecond-Long Balanced Mobilities, and Slow Recombination. *J. Am. Chem. Soc.* **2014**, *136*, 5189−5192.
(16) Johnston, M. B.; Herz, L. M. Hybrid Perovskites for Photovoltaics: Charge-Carrier Recombination, Diffusion, and Radiative Efficiencies. *Acc. Chem. Res.* **2016**, *49*, 146−154.
(17) Snaith, H. J.; Abate, A.; Ball, J. M.; Eperon, G. E.; Leijtens, T.; Noel, N. K.; Stranks, S. D.; Wang, J. T.-W.; Wojciechowski, K.; Zhang, W. Anomalous Hysteresis in Perovskite Solar Cells. *J. Phys. Chem. Lett.* **2014**, *5*, 1511−1515.
(18) Kim, H.-S.; Jang, I.-H.; Ahn, N.; Choi, M.; Guerrero, A.; Bisquert, J.; Park, N.-G. Control of *I*−*V* Hysteresis in $CH_3NH_3PbI_3$ Perovskite Solar Cell. *J. Phys. Chem. Lett.* **2015**, *6*, 4633−4639.
(19) Chen, B.; Yang, M.; Priya, S.; Zhu, K. Origin of *J*−*V* Hysteresis in Perovskite Solar Cells. *J. Phys. Chem. Lett.* **2016**, *7*, 905−917.
(20) Noh, J. H.; Im, S. H.; Heo, J. H.; Mandal, T. N.; Seok, S. I. Chemical Management for Colorful, Efficient, and Stable Inorganic-Organic Hybrid Nanostructured Solar Cells. *Nano Lett.* **2013**, *13*, 1764−1769.
(21) Niu, G.; Li, W.; Meng, F.; Wang, L.; Dong, H.; Qiu, Y. Study on the Stability of $CH_3NH_3PbI_3$ Films and the Effect of Post-Modification by Aluminum Oxide in All-Solid-State Hybrid Solar Cells. *J. Mater. Chem. A* **2014**, *2*, 705−710.
(22) Niu, G.; Guo, X.; Wang, L. Review of Recent Progress in Chemical Stability of Perovskite Solar Cells. *J. Mater. Chem. A* **2015**, *3*, 8970−8980.
(23) Egger, D. A.; Kronik, L. Role of Dispersive Interactions in Determining Structural Properties of Organic-Inorganic Halide Perovskites: Insights from First-Principles Calculations. *J. Phys. Chem. Lett.* **2014**, *5*, 2728−2733.
(24) Li, J.; Rinke, P. Atomic Structure of Metal-Halide Perovskites from First Principles: The Chicken-and-Egg Paradox of the Organic-Inorganic Interaction. *Phys. Rev. B: Condens. Matter Mater. Phys.* **2016**, *94*, 045201.
(25) Brivio, F.; Walker, A. B.; Walsh, A. Structural and Electronic Properties of Hybrid Perovskites for High-Efficiency Thin-Film Photovoltaics from First-Principles. *APL Mater.* **2013**, *1*, 042111.
(26) Frost, J. M.; Butler, K. T.; Brivio, F.; Hendon, C. H.; van Schilfgaarde, M.; Walsh, A. Atomistic Origins of High-Performance in Hybrid Halide Perovskite Solar Cells. *Nano Lett.* **2014**, *14*, 2584−2590.
(27) Leguy, A. M. A.; Frost, J. M.; McMahon, A. P.; Garcia Sakai, V.; Kochelmann, W.; Law, C. H.; Li, X.; Foglia, F.; Walsh, A.; O'Regan, B. C.; et al. The Dynamics of Methylammonium Ions in Hybrid Organic-Inorganic Perovskite Solar Cells. *Nat. Commun.* **2015**, *6*, 7124.
(28) Meloni, S.; Moehl, T.; Tress, W.; Franckevičius, M.; Saliba, M.; Lee, Y. H.; Gao, P.; Nazeeruddin, M. K.; Zakeeruddin, S. M.; Rothlisberger, U.; et al. Ionic Polarization-Induced Current-Voltage Hysteresis in $CH_3NH_3PbX_3$ Perovskite Solar Cells. *Nat. Commun.* **2016**, *7*, 10334.
(29) Wasylishen, R. E.; Knop, O.; MacDonald, J. B. Cation Rotation in Methylammonium Lead Halides. *Solid State Commun.* **1985**, *56*, 581−582.
(30) Onoda-Yamamuro, N.; Matsuo, T.; Suga, H. Dielectric Study of $CH_3NH_3PbX_3$ (X = Cl,Br,I). *J. Phys. Chem. Solids* **1992**, *53*, 935−939.
(31) Mosconi, E.; Quarti, C.; Ivanovska, T.; Ruani, G.; De Angelis, F. Structural and Electronic Properties of Organo-Halide Lead Perovskites: A Combined IR-Spectroscopy and *Ab Initio* Molecular Dynamics Investigation. *Phys. Chem. Chem. Phys.* **2014**, *16*, 16137−16144.
(32) Chen, T.; Foley, B. J.; Ipek, B.; Tyagi, M.; Copley, J. R. D.; Brown, C. M.; Choi, J. J.; Lee, S.-H. Rotational Dynamics of Organic Cations in the $CH_3NH_3PbI_3$ Perovskite. *Phys. Chem. Chem. Phys.* **2015**, *17*, 31278−31286.
(33) Lee, J.-H.; Bristowe, N. C.; Bristowe, P. D.; Cheetham, A. K. Role of Hydrogen-Bonding and Its Interplay with Octahedral Tilting in $CH_3NH_3PbI_3$. *Chem. Commun.* **2015**, *51*, 6434−6437.
(34) Frick, B.; Combet, J.; van Eijck, L. New Possibilities with Inelastic Fixed Window Scans and Linear Motor Doppler Drives on

DOI: 10.1021/acs.jpclett.8b01321
J. Phys. Chem. Lett. 2018, 9, 3969−3977

High Resolution Neutron Backscattering Spectrometers. *Nucl. Instrum. Methods Phys. Res., Sect. A* **2012**, *669*, 7−13.
(35) Arrighi, V.; Higgins, J. S.; Burgess, A. N.; Howells, W. S. Rotation of Methyl Side Groups in Polymers: A Fourier Transform Approach to Quasielastic Neutron Scattering. 1. Homopolymers. *Macromolecules* **1995**, *28*, 2745−2753.
(36) Lahnsteiner, J.; Kresse, G.; Kumar, A.; Sarma, D. D.; Franchini, C.; Bokdam, M. Room-Temperature Dynamic Correlation Between Methylammonium Molecules in Lead-Iodine Based Perovskites: An *Ab Initio* Molecular Dynamics Perspective. *Phys. Rev. B: Condens. Matter Mater. Phys.* **2016**, *94*, 214114.
(37) Perdew, J. P.; Burke, K.; Ernzerhof, M. Generalized Gradient Approximation Made Simple. *Phys. Rev. Lett.* **1996**, *77*, 3865−3868.
(38) Tkatchenko, A.; Scheffler, M. Accurate Molecular Van Der Waals Interactions from Ground-State Electron Density and Free-Atom Reference Data. *Phys. Rev. Lett.* **2009**, *102*, 073005.
(39) van Lenthe, E.; Baerends, E. J.; Snijders, J. G. Relativistic Regular Two-Component Hamiltonians. *J. Chem. Phys.* **1993**, *99*, 4597−4610.
(40) Perdew, J. P.; Ernzerhof, M.; Burke, K. Rationale for Mixing Exact Exchange with Density Functional Approximations. *J. Chem. Phys.* **1996**, *105*, 9982−9985.
(41) Blum, V.; Gehrke, R.; Hanke, F.; Havu, P.; Havu, V.; Ren, X.; Reuter, K.; Scheffler, M. Ab Initio Molecular Simulations with Numeric Atom-Centered Orbitals. *Comput. Phys. Commun.* **2009**, *180*, 2175−2196.
(42) Havu, V.; Blum, V.; Havu, P.; Scheffler, M. Efficient $O(N)$ Integration for All-Electron Electronic Structure Calculation Using Numeric Basis Functions. *J. Comput. Phys.* **2009**, *228*, 8367−8379.
(43) Ren, X.; Rinke, P.; Blum, V.; Wieferink, J.; Tkatchenko, A.; Sanfilippo, A.; Reuter, K.; Scheffler, M. Resolution-of-Identity Approach to Hartree-Fock, Hybrid Density Functionals, RPA, MP2, and *GW* with Numeric Atom-Centered Orbital Basis Functions. *New J. Phys.* **2012**, *14*, 053020.
(44) Levchenko, S. V.; Ren, X.; Wieferink, J.; Johanni, R.; Rinke, P.; Blum, V.; Scheffler, M. Hybrid Functionals for Large Periodic Systems in an All-Electron, Numeric Atom-Centered Basis Framework. *Comput. Phys. Commun.* **2015**, *192*, 60−69.
(45) Ceriotti, M.; Manolopoulos, D. E. Efficient First-Principles Calculation of the Quantum Kinetic Energy and Momentum Distribution of Nuclei. *Phys. Rev. Lett.* **2012**, *109*, 100604.
(46) Ceriotti, M.; More, J.; Manolopoulos, D. E. i-PI: A Python Interface for *Ab Initio* Path Integral Molecular Dynamics Simulations. *Comput. Phys. Commun.* **2014**, *185*, 1019−1026.
(47) Novel Materials Discovery (NOMAD) repository, DOI: 10.17172/NOMAD/2018.04.25-1.
(48) Demaison, J.; Maes, H.; Van Eijck, B. P.; Wlodarczak, G.; Lasne, M. C. Determination of the Moment of Inertia of Methyl Groups: Analysis of the Millimeterwave Spectra of *cis*-Propanal and Methylthioethyne. *J. Mol. Spectrosc.* **1987**, *125*, 214−224.

DOI: 10.1021/acs.jpclett.8b01321
J. Phys. Chem. Lett. 2018, 9, 3969−3977